# Structure and Microdeformation of (iPP/iPP-*g*-MA)−PA6 Reaction Bonded Interfaces

**Christopher J. G. Plummer* and Hans-Henning Kausch**

*Laboratoire de Polymères, École Polytechnique Fédérale de Lausanne, Lausanne CH-1015, Switzerland*

**Costantino Creton**

*Laboratoire de Physico-Chimie Structurale et Macromoléculaire, ESPCI, rue Vauquelin, 7231 Paris Cedex 05, France*

**Frédérique Kalb and Liliane Léger**

*Laboratoire de Physique de la Matière Condensée, URA CNRS 792, College de France, 11, place Marthelin-Berthelot, 75231 Paris Cedex 05, France*

*Received December 23, 1997; Revised Manuscript Received May 13, 1998*

ABSTRACT: Transmission electron microscopy has been used in conjunction with $RuO_4$ staining to investigate the structure of (iPP/iPP-*g*-MA)−PA6 reaction bonded interfaces and microdeformation at interfaces which had failed by crack propagation along the interface. In relatively weak interfaces, the crack tip was preceded by a single, well-defined crazelike fibrillar deformation zone on the iPP/iPP-*g*-MA side of the interface, with fibril diameters of between 10 and 15 nm. The crack tip itself also propagated along the interface, providing some justification for the extension of established models for interfacial failure in glassy polymers to the present case of two semicrystalline polymers. In stronger interfaces, however, considerable diffuse deformation was observed to accompany crack propagation. This was accounted for by the deeper penetration of the damage zone into the iPP/iPP-*g*-MA, into regions where the microstructure was less well ordered than immediately adjacent to the interface. This transition from a well-defined to a diffuse damage zone may modify the relationship between the local interfacial strength and the global fracture toughness.

## Introduction

The present report describes work intended to clarify the nature of microdeformation ahead of and around the crack tip during crack propagation along reaction bonded interfaces between isotactic polypropylene (iPP)/maleic anhydride functionalized isotactic polypropylene (iPP-*g*-MA) blends and polyamide 6 (PA6). There exists a considerable body of recent experimental work concerning fracture of interfaces between immiscible amorphous glassy polymers.[1−10] Much of this work has been successfully interpreted in terms of recent theoretical advances on the microdeformation mechanisms occurring at the crack tip[11−14] and on the effects of mixed-mode crack propagation at an interface.[15,16] However, the mechanical behavior of interfaces between two immiscible *semicrystalline* polymers is less well characterized. It was therefore hoped that direct observation by transmission electron microscopy (TEM) of local structure and crack tip deformation mechanisms associated with such an interface would be useful in assessing the extent to which the aforementioned models for glassy polymers might be used to interpret measurements of the macroscopic fracture toughness (quantified here in terms of the critical strain energy release rate, $G_c$, for mode I crack propagation along the interface).

The report is organized as follows. In the remainder of this introduction a brief description is given of those aspects of cohesive and interfacial failure in glassy polymers which are pertinent to the subsequent discussion. This is followed by a summary of the results of previous investigations into the fracture behavior of reaction bonded (iPP/iPP-*g*-MA)−PA6 interfaces as a function of sample preparation conditions.[17,18] A microscopic investigation of the microstructure and microdeformation behavior at (iPP/iPP-*g*-MA)−PA6 interfaces is then presented, and the earlier results are reassessed in terms of the possible relevance of established models for bonded interfaces in amorphous glassy polymers.

**Cohesive and Interfacial Failure in Glassy Polymers.** In constrained geometries, such as at crack tips in relatively thick samples, flexible, un-cross-linked or lightly cross-linked amorphous glassy polymers generally deform by crazing. Craze microstructures have been intensively studied for many years by TEM and X-ray scattering.[19−24] It has been established, for example, that the characteristic dimensions of the internal structure of crazes obtained by deforming films thin enough to be electron transparent in a conventional TEM are consistent with those inferred from small-angle X-ray scattering of crazes in much thicker samples.[22,24] It is with some justification, therefore, that the results of TEM and low angle electron diffraction (LAED) studies of thin film crazes are invoked when considering the behavior of crack tip crazes in bulk tests. A particularly important observation in the present context is that of numerous cross-tie fibrils running perpendicular to and linking the main fibrils.[25−28] These cross-tie fibrils permit stress transfer within the craze in directions parallel to the craze faces. This can in turn give rise to a local stress concentration at the

* To whom correspondence should addressed.

S0024-9297(97)01852-4 CCC: $15.00 
Published on Web 08/21/1998

tip of a crack propagating through the craze, even if it is assumed that the stress normal to the craze faces is constant and equal to the fibril drawing stress.[11]

By considering a craze containing cross-tie fibrils to behave as an orthotropic linear elastic body, Brown expressed the global critical strain energy release rate, $G_c$, associated with a mode I crack moving perpendicular to the main fibril direction in a long craze, and under small scale yielding conditions, as

$$G_c = \frac{2\pi D_o(1 - 1/\lambda)}{S_c}\alpha^{1/2}(\Sigma f_s)^2 \qquad (1)$$

where $f_s$ is the force to break or disentangle a polymer chain, $\Sigma$ is the number of load bearing polymer strands crossing a planar surface of unit area within the undeformed polymer, $\alpha$ is an "elastic anisotropy factor" which is estimated to be about 40 for a PMMA craze, $\lambda$ is the draw ratio of the craze fibrils, $S_c$ is the draw stress of the craze fibrils, and $D_o$ is the fibril spacing.[11] Equation 1 has since been derived from more detailed micromechanical modeling[14] and is important in that it provides a direct link between the macroscopic quantity $G_c$ and the microscopic quantities $f_s$, $\Sigma$, $\lambda$, and $\alpha$, all of which may be measured, or at least estimated. However, it should be noted that eq 1 depends on the assumption that the craze can be treated as a continuum, and hence overestimates $G_c$ for weak interfaces.[12]

In a homogeneous glassy amorphous polymer, it is frequently assumed that

$$\Sigma = \frac{\nu_e d_e}{2} \qquad (2)$$

where $\nu_e$ is the entanglement density and $d_e$ is the entanglement spacing.[21,22] As well as giving the correct order of magnitude for $G_c$ in PMMA, when combined with eq 2 and models for dilution of the entanglement network owing to craze induced scission,[11] eq 1 accounts at least in part for the observed dependence of $G_c$ on the molecular weight in PMMA.[29]

It should be emphasized that the rupture of the craze fibrils consumes very little energy itself. However, the ultimate strength of the fibrils controls the maximum craze width and hence the total amount of crack tip dissipation owing to fibril drawing. Although the precise form of eq 1 is not expected to be applicable to cases of multiple crazing at the crack tip (as is usually observed in PS, for example) or mixed crazing and shear, the idea that the strength of individual polymer ligaments at the crack tip controls the dimensions of the damage zone should remain valid, serving to underline the importance of entanglement, not only for craze formation, but also for ultimate failure.

Compatibilization of interfaces between immiscible amorphous polymers often involves the addition of suitable block or random copolymers to the blend or interface.[4−9] As long as the molecular weights of the respective blocks or copolymers are sufficient to form entanglements on either side of the interface, this can also provide a means of varying $\Sigma$ systematically, since the concentration of block copolymer at the interface can usually be controlled. In such studies the total number of connecting molecules spanning unit area of the interface has been varied by depositing a film of the compatibilizer of known thickness on the surface of one component.[1,2,5,8,10,30−32] After heat treatment, allowing for the local reorganization of the block copolymer at the interface in a brush configuration, $\Sigma$ can be estimated directly, since $\Sigma$ represents the number of load bearing chains spanning the interface and only the block copolymer chains provide load bearing strands at interfaces between very immiscible polymers. It should be pointed out that $\Sigma$ cannot be increased indefinitely with the amount of copolymer at the interface, since homopolymer chains will eventually be expelled from the copolymer brush or microphase separation will intervene above a certain saturation threshold, depending on the molecular weight of the blocks. When the molecular weight of the blocks is larger than the average molecular weight between entanglements of both homopolymers (preventing simple chain pullout) and for sufficiently large $\Sigma$, crack advance along the interface is preceded by formation of a single craze on the side of the interface which has the lower crazing stress. For $M_n > 5M_e$, $G_c$ is found to scale as $\Sigma^2$, consistent with eq 1,[1] and to be approximately independent of molecular weight (suggesting chain scission to dominate the final rupture process in the craze fibrils). However, for smaller values of $M_n$, $\Sigma$ must be corrected to account for the presence of chain ends, which decrease the effective areal density of load-bearing strands.[29]

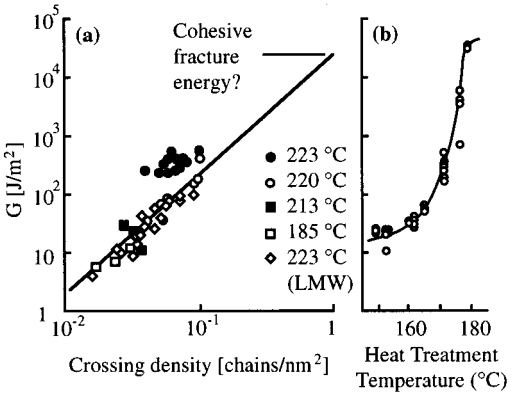


**Figure 1.** (a) The critical strain energy release rate, $G_c$, as a function of $\Sigma$ in (iPP/iPP-*g*-MA)−PA6 heat treated at different times and temperatures (after Boucher et al.;[18] for the iPP-*g*-MA, $M_n$ = 43 000 g mol$^{-1}$ except for the samples designated LMW, for which $M_n$ = 22 600 g mol$^{-1}$); (b) $G_c$ as a function of heat treatment temperature in diffusion bonded iPP−iPP interfaces (after Smith et al.[34]).

**(iPP/PP-*g*-MA)−PA6 Reaction Bonded Interfaces.** $G_c$ has also been reported to scale with $\Sigma^2$ in semicrystalline (iPP/5 wt % iPP-*g*-MA)−PA6 interfaces.[17,18] Compatibilization of these interfaces is assured by reaction bonding at temperatures above the melting point of the iPP/iPP-*g*-MA. The maleic anhydride groups of the iPP-*g*-MA functionalized iPP react with the $NH_2$ end groups of the PA-6 to form a copolymer in situ at the interface. In this case, the rate of copolymer formation and hence the value of $\Sigma$ after a given heat treatment time was controlled by the rate of diffusion of the iPP-*g*-MA through the majority iPP component.[17] This is not a general rule, however. The effective crossing density can be estimated by dissolving away the free PA6 from bonded (iPP/iPP-*g*-MA)−PA6 plaques and measuring the amount of PA6 which remains attached to the iPP.[18] Figure 1a shows $G_c$ for crack propagation along interfaces heat treated at different temperatures, expressed as a function of $\Sigma$ determined in this way. In this double-log plot, most

of the data lie on a straight line with a slope of approximately 2, implying $G_c$ to scale as $\Sigma^2$. However, it is significant that for the highest heat treatment temperature (223 °C), in samples containing iPP-*g*-MA with $M_n = 43\,000$ g mol$^{-1}$ and a polydispersity of 3.3, $G_c$ is about 4 times larger than for samples heat treated at lower temperatures, for any given $\Sigma$, although there is considerable scatter in this regime. Curiously, samples containing iPP-*g*-MA with $M_n = 22\,600$ g mol$^{-1}$ and a polydispersity of 2.7 heat treated at 223 °C do not show higher $G_c$ than samples with the same $\Sigma$ but heat treated at lower temperatures.[18] This result implies some sort of molecular weight dependent molecular interaction between the block copolymer and the iPP homopolymer and/or segregation effects. For example, the difference in behavior between the short ($M_n = 22\,600$ g mol$^{-1}$) and long (43 000 g mol$^{-1}$) PP-*g*-MA chains could be due to differences in the proportion of chains tethered to the PA-6 which are too short to entangle effectively. This hypothesis is plausible, given the polydisperse nature of the polymers and an estimated entanglement molecular weight of between 3000 and 4000 g mol$^{-1}$ for iPP. Indeed the average molecular weight of the tethered chains may also differ from the average molecular weight of the PP-*g*-MA dissolved in the bulk iPP. Alternatively, the molecular weight distribution of the tethered chains may influence the kinetics of cocrystallization with the bulk iPP during the cooling of the assembly. In either case, segregation of low molecular weight chains to or away from the interface could influence the overall adhesion, although at present we have little basis for further speculation on this point.

$\Sigma$ in all of these interfaces saturates at about 0.1 nm$^{-2}$, which corresponds to the point at which the chains tethered to the interface begin to overlap, inhibiting further reaction (assuming the interface to remain stable against formation of lamellar or micellar structures) and thus limiting the range of $\Sigma$ over which eq 1 can be tested by this technique. However, since analysis of the fracture surfaces and the measurement of the respective yield stresses of i-PP and PA-6 indicate that the crack tip deformation occurs on the iPP/iPP-*g*-MA side of the interface,[18] one might consider cohesive failure of pure iPP to be representative of the limiting behavior at high $\Sigma$. A rough estimate of the effective value of $\Sigma$ in pure iPP is $d_e\nu_e/2 \sim 1$ nm$^{-2}$, as in a glassy polymer[33] (this is arguably an oversimplification: although the original crystalline structure is destroyed during micronecking, crystallinity in the deformed regions contributes to load bearing and indeed is necessary to stabilize the entanglement network). The corresponding value of $G_c$ obtained by extrapolating the curve in Figure 1a is about $2 \times 10^5$ J m$^{-2}$, which is of the same order of magnitude as the highest experimental values of $G_c$ measured in diffusion bonded iPP−iPP interfaces by Smith et al., as shown in Figure 1b.[34] It has nevertheless been pointed out that the experimental data for the (iPP/iPP-*g*-MA)−PA6 interfaces would be inconsistent with eq 1 for any reasonable choice of parameters, if the effective craze fibril size and separation in iPP were of the order of 0.1 $\mu$m, a value which is sometimes cited in the literature.[18,35−37] One of the primary aims of the present work was therefore to investigate the internal structure of the crack tip damage zone with a view to obtaining precise data for these quantities.

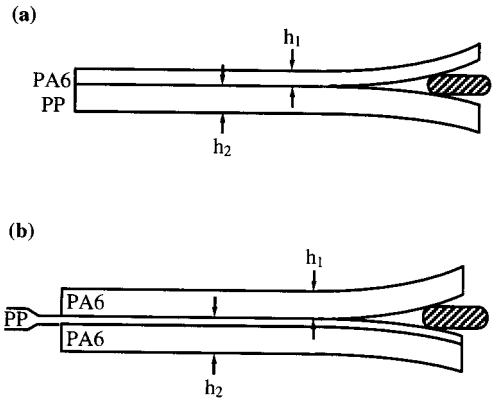


**Figure 2.** Sample geometries used for fracture toughness testing: (a) for $G_c \leq 140$ J m$^{-2}$ and (b) for $G_c \geq 140$ J m$^{-2}$.

## Experimental Section

The materials to be described in what follows were available in the form of extruded sheets of a commercial PA6 (from BASF) with $M_n = 17\,000$ g mol$^{-1}$, a polydispersity of 2, and an average of one $NH_2$ end group per chain, a blend of a commercial iPP (from APRYL) with $M_n = 57\,000$ g mol$^{-1}$, a polydispersity of 4.8, and a tacticity of 95%, and 5 wt % iPP-*g*-MA (from ATOCHEM) with $M_n = 43\,000$ g mol$^{-1}$, a polydispersity of 3.3, and an average of one maleic anhydride group per chain. The detailed procedure for the fabrication of the samples and their characterization (measurement of $G_c$ and of $\Sigma$) has been described elsewhere.[17] We therefore restrict ourselves to a brief summary of those aspects which are pertinent to the present investigation. The samples were prepared by clamping together sheets of PA6 and the iPP/iPP-*g*-MA blend in an airtight, Teflon-lined mold under slight pressure and subsequent heating of the molds in a temperature-controlled oven to various temperatures between 185 and 223 °C (a temperature range above the melting temperature of PP but below that of PA6). The thickness ($h$) of the polymer on each side of the interface was adjusted by using an appropriate number of sheets. In general, the total sample thicknesses ($h_{iPP/iPP\text{-}g\text{-}MA} + h_{PA6}$) were between 1.6 and 3.4 mm. Two geometries were used: for samples with measured fracture toughnesses below 140 J m$^{-2}$, we used the simple geometry shown in Figure 2a (the total sample thickness was increased as the energy of adhesion increased, to increase the crack length). Above 140 J m$^{-2}$, use was made of a "sandwich" geometry (Figure 2b), to minimize problems arising from the ductility of the iPP/iPP-*g*-MA.

The fracture toughness ($G_c$) of each sample was measured by using an asymmetric double cantilever beam (ADCB) test as described previously.[17] A blade of thickness $\Delta$ was inserted into the interface between the iPP/iPP-*g*-MA and PA6, and was pushed into the sample at a velocity of 3 $\mu$m/s. The crack length, $a$, was measured for every millimeter that the blade advanced, using a videocamera. The crack length and its standard deviation were determined from at least 10 video frames. $G_c$ was then obtained from the crack length and the geometrical parameters using a method based on Kanninen's analysis.[17] The ratio $h_{iPP/iPP\text{-}g\text{-}MA}/h_{PA6}$ was adjusted in order to avoid the crack deviation into the more ductile material (iPP/iPP-*g*-MA, in this case).

Two basic techniques were used for the microstructural investigation: (i) in situ deformation of unstained thin sections mounted on copper grids; (ii) $RuO_4$ staining and room-temperature thin sectioning with the Reichert Jung Ultracut-E ultramicrotome and a Diatome 45° diamond knife.

The first method has been used in the studies of glassy amorphous heterogeneous interfaces referred to in the Introduction, providing a means of identifying which side of the interface deforms most readily during crack propagation along the interface and the nature of the deformation (crazing, simple cleavage, or other).[8,31,32] In the present case, 100−200 nm thick sections of about 1 mm$^2$ in total area, containing

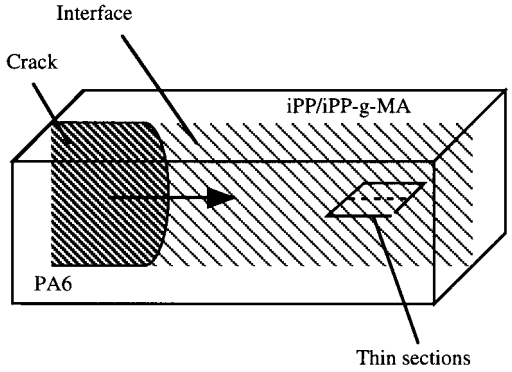


**Figure 3.** Sketch of the sectioning procedure for the preparation of thin films.

bonded (iPP/iPP-*g*-MA)−PA6 interfaces, were prepared either at room temperature or at −100 °C. Representative samples were poststained in the vapor of a freshly prepared $RuO_4$ solution (see below) in order to check that the lamellar morphology in the iPP/iPP-*g*-MA remained substantially intact after sectioning. The sections were generally taken parallel to the crack propagation direction in the bulk tests and perpendicular to the interface, with the cutting direction along the interface (see Figure 3). They were picked up on 200 mesh rectangular copper grids so that the interface lay along the diagonals of the grid squares. After drying, a small rectangular strip containing a given thin section was cut from the grid such that the long sides of the rectangle were perpendicular to the interface. This strip was then strained in the direction perpendicular to the interface at 0.1 mm/min at room temperature. Since this direction was also along the grid diagonals, the sample was essentially deformed in uniaxial tension normal to the interface and underwent some buckling at high strains. Once deformed, the sections were observed on the Phillips EM 300 TEM at 100 kV at magnifications of between 10000X and 20000X, and beam damage was monitored in diffraction mode.

For microstructural investigation of undeformed samples, a trimmed block containing the interface was placed in a freshly prepared $RuO_4$ solution, made from 200 mg of $RuCl_3 \cdot 3H_2O$ in 10 mL of 5% aqueous NaClO,[38] and left overnight. Although this was adequate for staining of the iPP side of the interface, the stain etched away the original PA6 surface, while at the same time penetrating less far into the PA6 than into the iPP/iPP-*g*-MA. Thus, although obtaining good quality sections with good lamellar contrast in the iPP/iPP-*g*-MA was relatively straightforward, simply involving removal of a surface layer of about 1 $\mu$m in thickness from the sample prior to thin sectioning, it was more difficult to obtain stained sections of the PA6. Moreover, poststaining of the sections proved disappointing, as did staining with phosphotungstic acid. With some perseverance, sections showing lamellar detail on both sides of the interface could be obtained, but it is acknowledged that the present method leaves room for improvement (one might envisage heating the samples above the $T_g$ of the PA6 in order to encourage diffusion of the $RuO_4$ into the nylon side of the sample or staining in the vapor phase using stronger solutions of $RuO_4$ in order to limit degradation of the PA6 surface layer). In what follows, therefore, we have concentrated on the iPP/iPP-*g*-MA side of the interface, which is in any case of most interest as far as microdeformation is concerned. Typical sections were between 50 and 100 nm thick and were picked up on carbon films and examined by using the Phillips EM 430 ST at 300 kV.

To investigate microdeformation at the tip of cracks propagating along the bulk interfaces, we adapted the method of Lutz,[39] who used $RuO_4$ staining to investigate microdeformation in iPP tensile test bars. Specimens which had undergone a certain amount of crack propagation (and for which $G_c$ had already been determined) were wedged open with a razor blade, and the razor blade was carefully pushed toward the crack tip, to cause a further limited amount of crack propagation just prior to embedding the sample in a low viscosity epoxy resin (with the razor blade left in place). The resin was left to cure at room temperature and then trimmed to provide a suitable surface for thin sectioning. Staining was again done by immersion in $RuO_4$ solution overnight. It was hoped this method would permit observation of the damage zone in its unrelaxed state, although in view of the long cure times (more than 12 h), some relaxation and possibly some additional propagation of the crack and/or the damage zone may have occurred during the cure. This should be borne in mind when considering the results to be described in the following section.

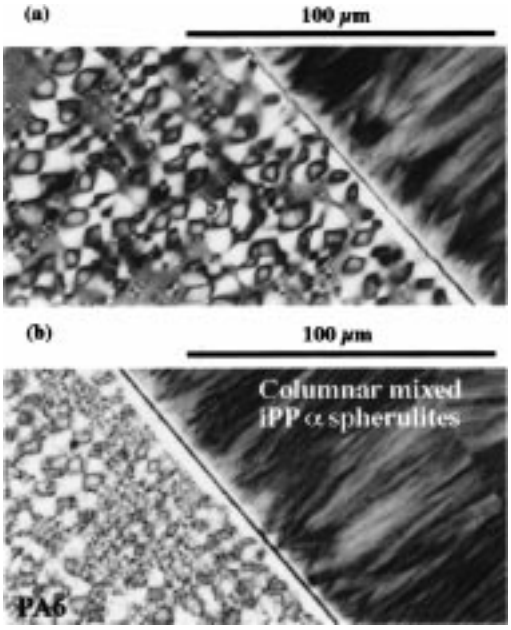


**Figure 4.** Optical micrographs of semithin sections between crossed polarizers (analyzer horizontal): (a) an interface heat treated at 215 °C for 840 min, $G_c = 50$ J m$^{-2}$; (b) an interface heat treated at 221 °C for 800 min, $G_c = 300$ J m$^{-2}$.

## Results

**Structure of Undeformed Interfaces.** Figure 4 shows optical micrographs of a relatively weak interface (heat treated at 215 °C for 840 min, $G_c = 50$ J m$^{-2}$) and a relatively strong interface (heat treated at 221 °C for 800 min, $G_c = 300$ J m$^{-2}$), taken using crossed polarizers to give birefringence contrast, with the analyzer direction horizontal. The microstructures of all the samples appeared very similar at this resolution as might be expected from their similar thermal histories. The heat treatment temperatures were generally above the equilibrium melting point of the usual monoclinic α form of iPP (185 °C),[40] and the cooling rate was 4 K/min in all cases. On the other hand, there was some evidence for recrystallization on the PA6 side of the interface heat treated at 221 °C, which is just above the peak temperature of the DSC melting endotherm for the PA6 as received, and indeed the heat treatment temperature of 215 °C used for the weaker interface also overlaps substantially with the low melting point tail of the endotherm.[18] Nevertheless, although substantial, particularly at 221 °C, melting of the PA6 was incomplete, the heat treatments resulting in an increase in the melting point, depending on the heat treatment temperature.[18]

The sign of the birefringence was determined by using a sensitive tint plate, indicating the PA6 spherulites to be positively birefringent, that is with the maximum in birefringence coinciding with optical axis (assumed to

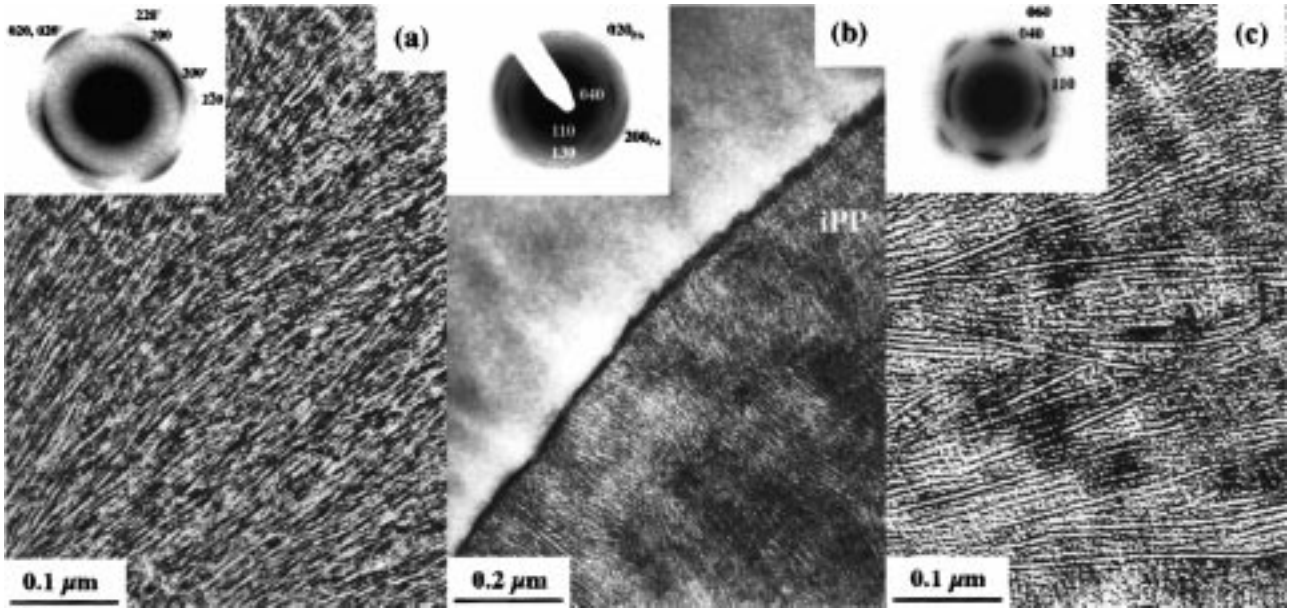


**Figure 5.** TEM micrographs from thin $RuO_4$ stained sections of a sample heat treated at 225 °C for 805 min with the corresponding DPs: (a) the bulk morphology of the PA6 side of the sample; (b) the interface; (c) the bulk morphology of the PP/iPP-*g*-MA)−PA6 side of the sample.

be parallel to the spherulite radii). As will be shown later, in PA6 the lamellae grew roughly along the spherulite radii, but the crystallographic orientation was such that the hydrogen bonding direction was also radial ([100] in the α PA6 monoclinic unit cell[41]), accounting for the positive birefringence in this case.[42] Well away from the interface, the microstructure of the iPP/iPP-*g*-MA essentially consisted of either slightly positively birefringent or "mixed" sections through α spherulites. In contrast with PA6, positive birefringence in iPP is generally identified with autoepitaxial nucleation of a significant population of lamellae growing approximately perpendicular to the radial lamellae, giving the well-known "cross-hatched" texture.[43−45] Mixed spherulites consist of multiple sectors containing either predominantly radially or predominantly tangentially oriented lamellae, giving a streaked appearance between cross-polarizers, and the Maltese cross typical of uniformly birefringent spherulites is absent.

Transcrystalline layers are visible in the Figure 4 on both the iPP/iPP-*g*-MA and the PA6 sides of the interface. For the most part, these layers showed the same optical properties as the respective spherulites. However, careful examination of the micrographs revealed a thin, apparently nonspherulitic, negatively birefringent layer of iPP/iPP-*g*-MA immediately adjacent to the interface (not to be confused with the dark Fresnel fringe visible at the interface in Figure 4). At about 1 $\mu$m from the interface, there was a transition zone marked by the nucleation of numerous mixed spherulites, although as may be seen in Figure 4a, some nucleation also occurred at the interface, resulting in discontinuities in the positively birefringent layer referred to above. The continued growth of these spherulite nuclei resulted in the formation of the remainder of transcrystalline layer, which extended to about 100 $\mu$m from the interface. Beyond this distance the texture consisted of equiaxed mixed spherulites, as mentioned earlier. Although sometimes associated with transcrystallinity in iPP, spherulites of the trigonal $\beta$ phase[46] typically accounted for less than 1% of the total area of the sections examined. When they were seen, it was generally at the interface between the transcrystalline and equiaxed zones, their being easily identifiable from their strong negative birefringence.

Such microstructures are characteristic of the flow-induced surface orientation and thermal gradients occurring during thermoforming. However, they were somewhat unexpected in the present case of very long heat treatments under quiescent conditions at temperatures above the equilibrium melting point and subsequent slow cooling. For the stronger interfaces, an adequate total sample thickness for the mechanical tests was often ensured by laminating several of the iPP/iPP-*g*-MA sheets. The interfaces between these sheets also showed a transcrystalline structure very similar to that at the interface with the PA6. This suggests that the final microstructures retain some memory of the original extrusion-induced structure, despite the severe heat treatments employed. Although it is hoped eventually to clarify the reasons for this with a view to gaining some degree of control over the microstructures in future experiments, the scope of the present work was limited to the characterization of samples used in previous studies, and so we shall not pursue this discussion here.

Figure 5 shows relatively low magnification highly defocused TEM images from different regions of a sample reacted for 805 min at 225 °C and sectioned in the same direction as the optical sections in Figure 4, along with the corresponding diffraction patterns (DPs). Figure 5a shows stained filiform α PA6 lamellae with undulating trajectories globally oriented along a spherulite radius. It was possible to obtain quasi-single-crystal microbeam DPs from the PA6 spherulites, but for larger areas (about 300 nm in diameter) the DPs typically showed reflectional symmetry about the radial [100] direction as shown in Figure 5a. Figure 5b shows the interface, highlighted by a dark band of relatively heavy staining, and the contrast between the (in this case unstained) PA6 and the iPP/iPP-*g*-MA, in which considerable lamellar detail is visible. The DP here was taken from a region straddling the interface, showing weak reflections from both the PA6 and the iPP α

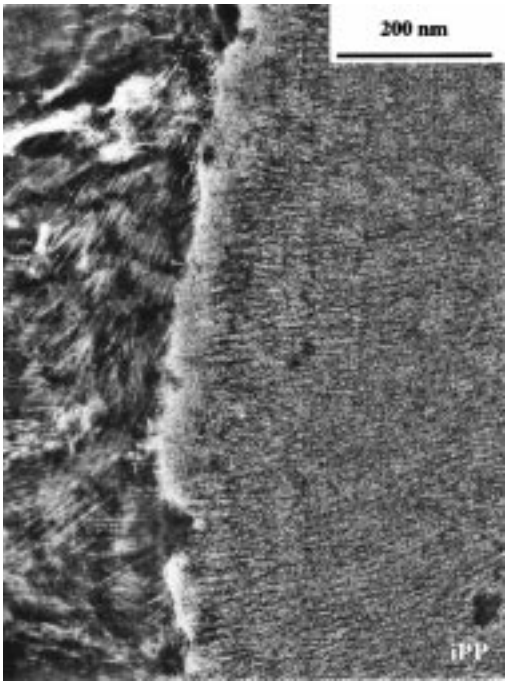


**Figure 6.** Detail from the interface in a relatively strongly stained section from the sample in Figure 5.

phases. This contrasts with DPs taken from well within the mixed transcrystalline region, such as shown in Figure 5c, in which strong reflections from the [001] zone were generally visible, with *a** parallel to the lamellar direction. It should be stressed that such DPs do not correspond to lamellar orientations giving pronounced crosshatched textures in the micrographs, since the *a* and *c* axes of the secondary lamellae giving rise to the crosshatched structure are respectively parallel to the *c* and *a* axes of the radial lamellae.[47] Thus if the trajectories of the two lamellar populations are in the plane of the section, it is the [010] direction which is parallel to the beam, and there are no strong low-order reflections in this orientation.

Figure 6 shows a more strongly stained section from the interface in Figure 5 in which lamellae on both sides of the interface are visible. For comparison, Figure 7 shows a section taken from deeper into the same sample, in which the PA6 is unstained. There was no apparent correlation in the lamellar orientation on either side of the interface and no suggestion of epitaxy, although epitaxy is known to occur in iPP growing on oriented PA films.[48] The interface was delineated by one or two dark bands in relatively lightly stained samples, regardless of the heat treatment temperature (Figure 7 provides an indication of the extent of surface roughness − it should be kept in mind that such images represent the projection of structure within a thickness of the order of 100 nm). These were replaced by a single relatively thick band in more heavily stained samples, extending into the PA6 (of the order of tens of nm). This was thought to be because stain diffusing through either the iPP/iPP-*g*-MA or the interface itself darkened adjacent regions of the PA6. Indeed some PA6 lamellae could occasionally be distinguished close to the interface in sections in which the bulk of the PA6 was unstained. In the section shown in Figure 6, heavy staining was generalized on the PA6 side of the interface obscuring, any preferential staining of this latter (the light, apparently amorphous layer on the iPP/iPP-*g*-MA side of the interface was thought to be an artifact, possibly due to deformation induced during sectioning, since it was not a general feature of more lightly stained sections). Images such as that in Figure 6 were exceptionally difficult to obtain, owing to the fragility of the heavily stained samples, and in general represented only small fragments of the original interface. For comparison, therefore, Figure 8 shows the microstructure of a (iPP/iPP-*g*-MA)−PA6 blend, processed well above the melting point of the PA6,[49] and from which it was somewhat easier to obtain micrographs in which all the phases were adequately stained (since we were not constrained to look at any particular part of the sections). On this basis, the absence of correlation between the lamellar

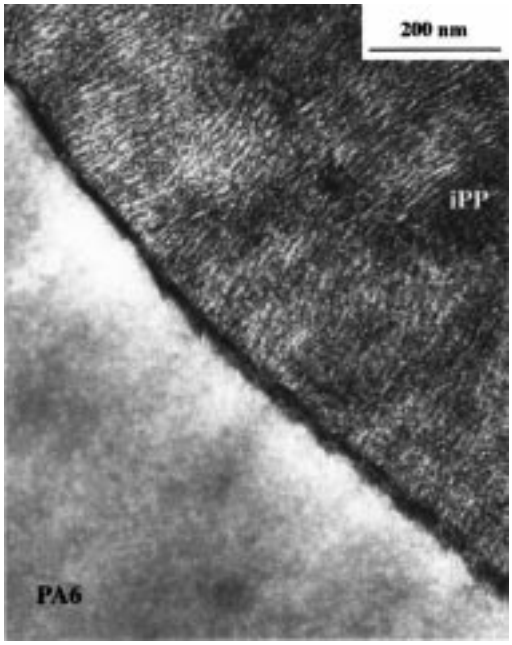


**Figure 7.** As Figure 6, but less strongly stained.

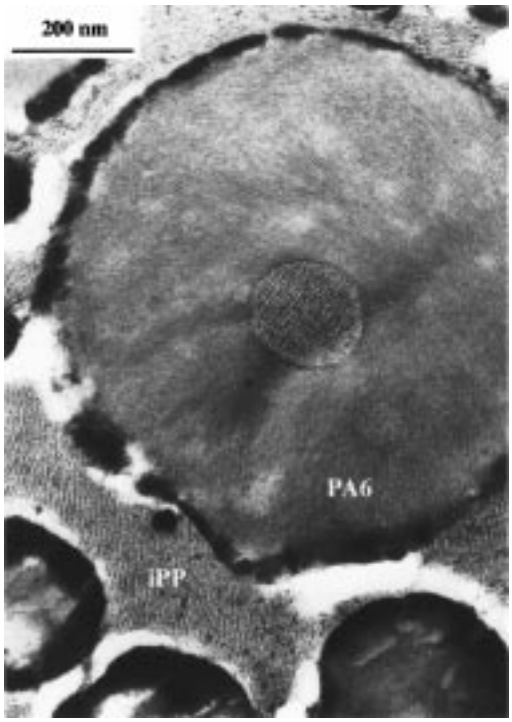


**Figure 8.** Thin $RuO_4$ stained section from a (iPP/iPP-*g*-MA)−PA6 blend, processed well above the melting point of the PA6.

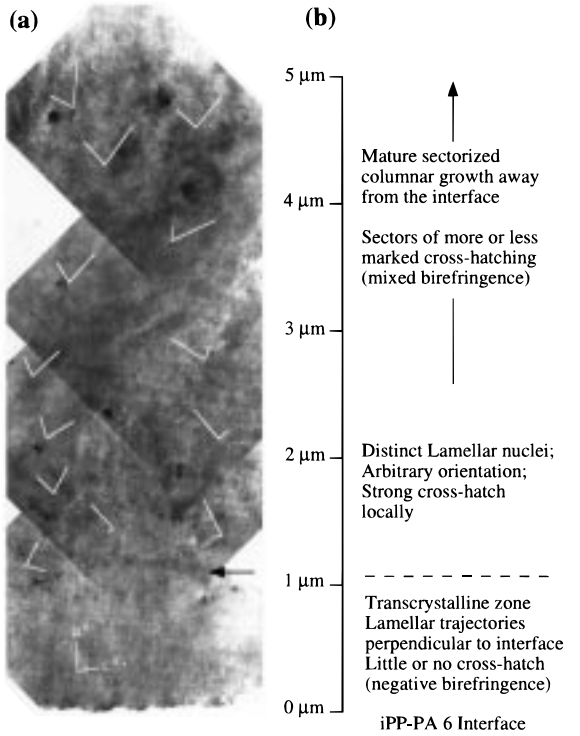


**Figure 9.** (a) Relatively low magnification TEM image of the iPP/iPP-*g*-MA side of the interface in Figures 5−7, showing part of the mixed transcrystalline zone, as well as the biaxially oriented layer, with an indication of the projections of the lamellar trajectories locally; (b) a schematic representation of the interfacial structure. The arrow in (a) indicates the slightly more heavily stained boundary between the biaxially oriented layer and the mixed zone.

trajectories on either side of the interface appears to be confirmed.

Within about 1 $\mu$m of the interface, in the region corresponding to the negatively birefringent layer observed optically in the iPP/iPP-*g*-MA, the lamellar trajectories were generally oriented perpendicular to the interface (as in Figure 6, for example). There was little apparent autoepitaxial growth in this region, as was confirmed by examining transverse sections. Moreover, DPs from the transverse sections were indicative of a biaxially oriented α crystallographic texture, with the *c* axis aligned parallel to the interface and *a** aligned normal to the interface, such that [010] was approximately parallel to the beam in Figure 5b (explaining the lack of strong α iPP reflections in the DP in this case). Figure 9 shows a lower magnification image of the iPP/iPP-*g*-MA side of the interface containing part of the mixed transcrystalline zone, as well as the biaxially oriented layer, with an indication of the projections of the lamellar trajectories locally. Beyond about 1 $\mu$m from the interface, regions of more pronounced crosshatching were typically observed, with differing lamellar orientations, corresponding to distinct spherulite nuclei (as inferred earlier from the optical micrographs in Figure 4). Further into the iPP/iPP-*g*-MA, in the region of "mature" transcrystalline growth, the trajectories of the primary lamellae were more uniformly oriented normal to the interface, owing to crowding and to the absence of further primary nucleation.

This structure, which is also shown schematically in Figure 9, was typical of all the samples investigated, including interfaces with $G_c$ as low as 20 J m$^{-2}$, and

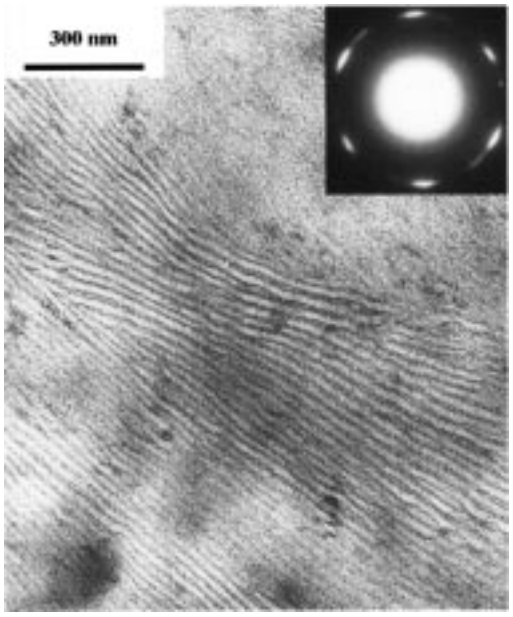


**Figure 10.** Thin $RuO_4$ stained section from part of a $\beta$ spherulite with the corresponding diffraction pattern.

indeed it was not possible to distinguish between the different samples on the basis of individual TEM micrographs of the iPP/iPP-*g*-MA close to the interface using the present sample preparation methods (although a slight increase in the thickness of the PA6 lamellae with increasing heat treatment temperature was discernible). Nevertheless, consistent with optical micrographs, in some sections crosshatched lamellae were seen at the interface itself, particular for the higher heat treatment temperatures. Moreover, the boundaries between regions of different structure and/or orientation frequently showed preferential staining, as shown in Figure 9, for example. Heavily stained sections tended to fracture along these boundaries, so that the biaxially oriented iPP/iPP-*g*-MA layer often remained attached to the PA6 in sections which had apparently failed along the interface during microtoming.

Consistent with the optical micrographs, there was little evidence from TEM for the presence of the $\beta$ phase in any of the sections investigated, although occasional $\beta$ spherulites were encountered in the regions of equiaxed spherulitic structure well beyond the interfaces. These were easily identifiable from their distinctive structure and DPs, as shown in Figure 10. Previous glancing angle X-ray investigations on similar samples by Boucher et al.[18] had shown the presence of the $\beta$ phase in the region near the interface. The reason for the discrepancy between the X-ray and TEM results is not yet known and a systematic comparison of both techniques on the same samples is under way to clarify the potential role of the iPP $\beta$ phase in these fracture experiments.

**Microdeformation in Thin Sections.** Figure 11 shows deformation at the interface in unstained thin sections taken from samples subjected to the heat treatments indicated and for which $G_c$ had been measured previously. In all cases deformation initiated at the interface and propagated into the iPP/iPP-*g*-MA side of the interface to give an asymmetric wedge-shaped deformation zone (DZ), which subsequently broke down at the interface to give a true crack. If this type of geometry is compared with the geometry of the DZ or

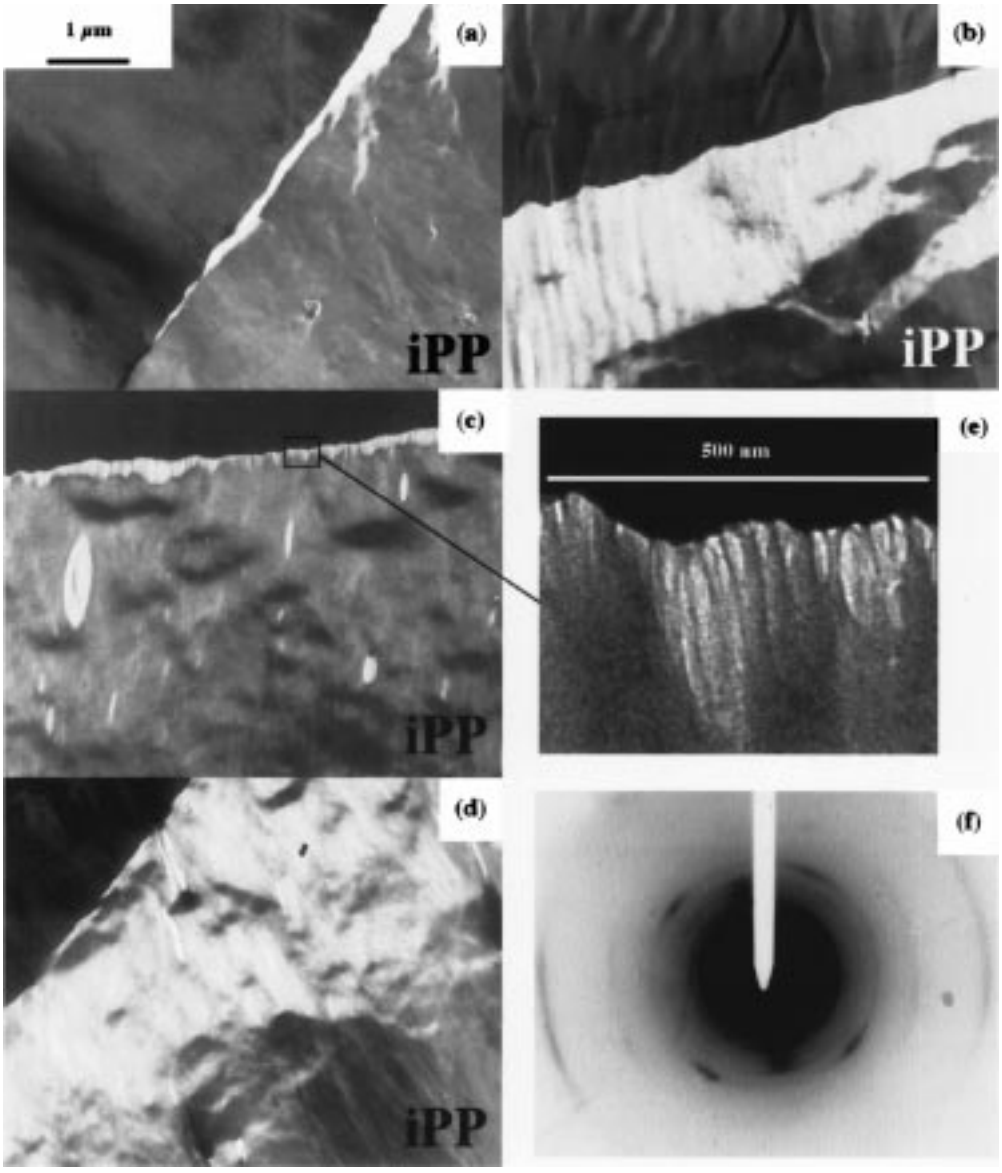


**Figure 11.** Deformation in unstained thin sections from interfaces bonded under different conditions: (a) 217 °C for 310 min, $G_c = 20$ J m$^{-2}$; (b) 225 °C for 840 min, $G_c = 75$ J m$^{-2}$; (c) 220 °C for 800 min, $G_c = 400$ J m$^{-2}$; (d) 225 °C for 805 min, $G_c = 700$ J m$^{-2}$. (e) Detail from the edge of the DZ in (c); (f) a DP taken from within the DZ (the deformation axis is approximately horizontal).

craze ahead of a propagating crack in a homogeneous polymer, it might best be described as a half-DZ, as sketched in Figure 12 (the application of eq 1 to this situation can then be justified by symmetry arguments). The interfaces corresponding to the lowest $G_c$ were generally observed to show far more limited deformation prior to failure than the stronger interfaces. Thus for the interface for which $G_c = 20$ J m$^{-2}$, the maximum width, $h_f$, of the DZ was about 1 $\mu$m, corresponding to an effective crack opening displacement $\delta = (1 - 1/\lambda)h_f = 0.75$ $\mu$m, using $\lambda = 4$ (see below).[33] Given a drawing stress, $S_c$, parallel to the lamellar direction of about 25 MPa, the critical crack opening displacement, $\delta_c$, corresponding to $G_c = 20$ J m$^{-2}$ would be 0.8 $\mu$m (using $G_c = S_c\delta_c$). For $G_c = 75$ J m$^{-2}$, $\delta_c \sim 3$ $\mu$m, which is again consistent with the observed $h_f$. However, for the stronger interfaces, it became difficult to estimate the effective overall widths of the DZs since the deformation was extremely diffuse, with several distinct DZs often forming within about 50 $\mu$m of the interface. Indeed some diffuse deformation was also visible at the low strength interfaces, as shown in Figure 11, with small

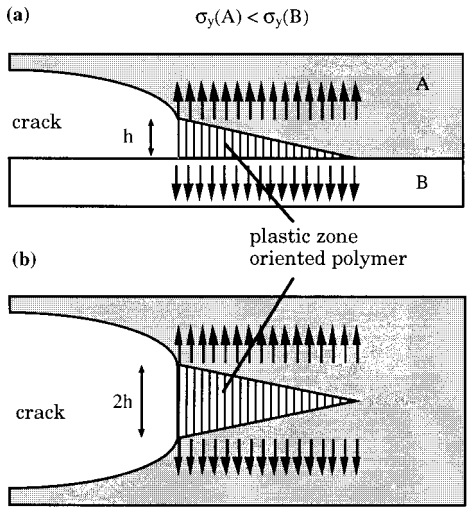


**Figure 12.** (a) Geometry of a half-crack/half-DZ propagating on one side of an asymmetric interface and (b) crack and DZ propagation in a homogeneous structure.

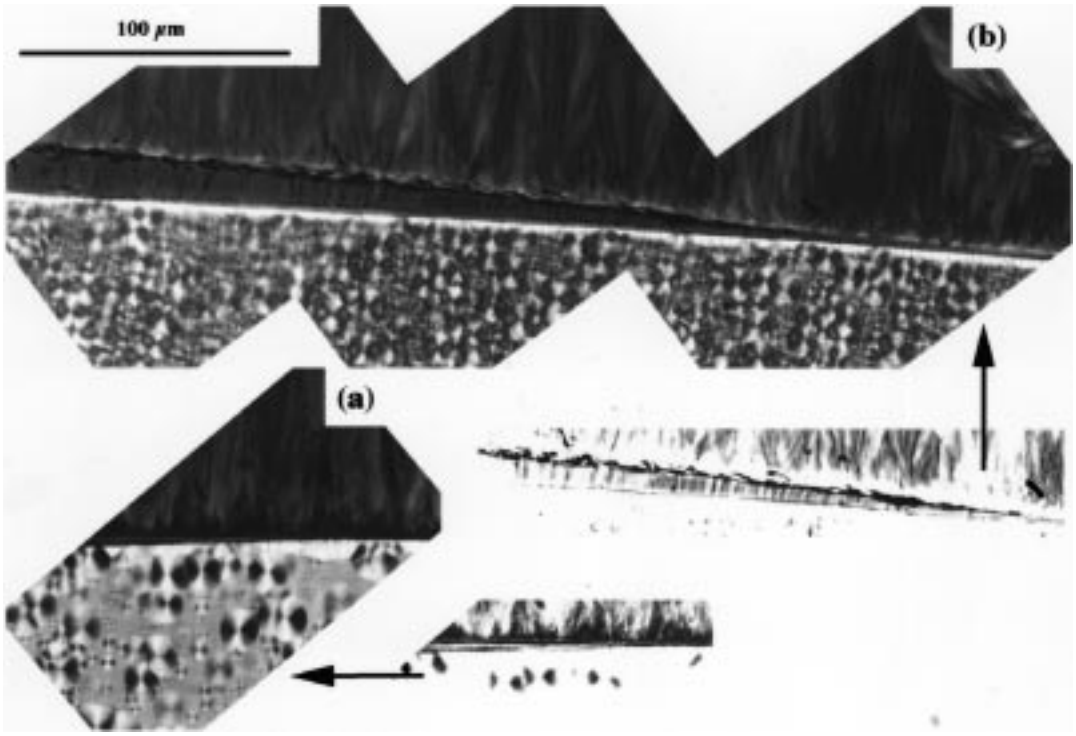


**Figure 13.** Optical micrographs as in Figure 4 but taken from the tip of a crack which had propagated some distance along the interface: (a) an interface heat treated at 215 °C for 840 min, $G_c = 50$ J m$^{-2}$; (b) an interface heat treated at 221 °C for 800 min, $G_c = 300$ J m$^{-2}$; the insets show phase contrast images in which the crack tip DZ is more clearly visible.

secondary DZs occasionally propagating along inclined trajectories with respect to the interface. However, it should be kept in mind that (i) the experimental conditions made precise control of the local stress state impossible in these experiments and (ii) there are no through thickness constraints in the thin film geometry, which may favor delocalization of micronecking to weak spots, such as spherulite boundaries (or damage induced during sectioning).

All the thin film DZs showed pronounced fiber DPs, identified with the so-called smectic phase (associated with shifts in certain of the *hk*0 *d* spacings with respect to those of the undeformed α structure). They did not show clear fibrillar textures, even in strongly defocused images, although pronounced voiding was often observed at the interface, as shown in Figure 11, suggestive of a mean fibril diameter of the order of 10 nm. This lack of extensive fibrillation/cavitation would be incompatible with localized crack tip deformation in a bulk sample, under small-scale yielding conditions, owing to the constraints due to the surrounding material on contraction normal to the draw direction (assuming conservation of volume during plastic deformation). This underlined the need to observe microdeformation in bulk samples directly. The observations in Figure 11 nevertheless provided some justification for assuming deformation to occur in the iPP/iPP-*g*-MA and breakdown to take place at the interface, as inferred previously from analysis of the fracture surface. It was also possible to estimate, $\lambda$, the draw ratio in the DZs, from the mass thickness contrast in the images. $\lambda$ was thus confirmed to be roughly equal to 4, consistent with previous measurements on melt recrystallized solution cast iPP films, where this value was identified with the natural draw ratio of the entanglement network.[33]

**Microdeformation in Bulk Samples.** Microdeformation in two samples with different interfacial strengths will be described in detail here, namely, the samples whose microstructures were shown in Figure 4. Figure 13 shows further optical micrographs, again taken with crossed polarizers, and showing crack-tip DZs in the deformed samples. For the interface with $G_c = 300$ J m$^{-2}$ a wedge-shaped DZ was clearly visible at the crack tip with an apparent maximum width of the order of 10 $\mu$m. Dark striations were also seen at the zone edge, suggesting deformation to have occurred beyond the boundary of the main DZ. No such striations were visible in the weaker interface, where the DZ itself was harder to distinguish, and its maximum width was estimated to be no more than a few micrometers.

Figure 14 is a low magnification image of part of the DZ in the stronger interface, taken close to the crack tip, and in which the positions of the PA6, the body of the main DZ, and the iPP/iPP-*g*-MA side of the interface are indicated. Little detail was visible within the main DZ, although close examination revealed a fibrillar texture (the presence of the epoxy appeared to inhibit staining within the DZ). On the other hand, considerable detail was observed at the edge of the DZ on the iPP/iPP-*g*-MA side of the interface. The edge of the DZ itself was strongly stained, highlighting the fibrillar structure, which had undergone a certain amount of relaxation during the sample preparation. Moreover, the striations seen in the optical micrographs just beyond the edge of the DZ were seen to correspond to a complex network of diffuse interlamellar deformation (including cavitation), secondary fibrillar DZs (shown in detail in Figure 15), and matrix shear. Also visible in Figure 14 is a localized region of coarse cavitation, associated with an inclusion present in the iPP/iPP-*g*-MA, which was thought to be due to the presence of a small amount of amorphous ethylene−propylene copolymer. Such inclusions were encountered in all the samples, but in insignificant proportions. Finally,

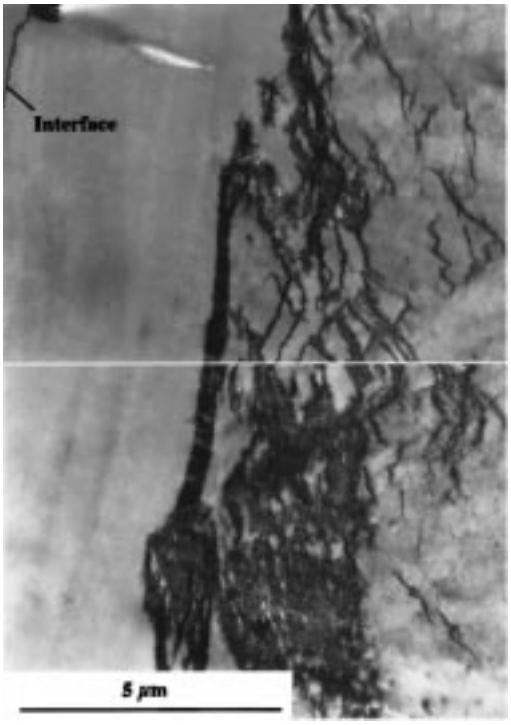


**Figure 14.** Relatively low magnification image of part of the DZ in the interface in Figure 13b. The position of the iPP/iPP-*g*-MA interface is as indicated (note that the interior of the main fibrillar deformation zone shows little contrast owing to lack of penetration of the stain).

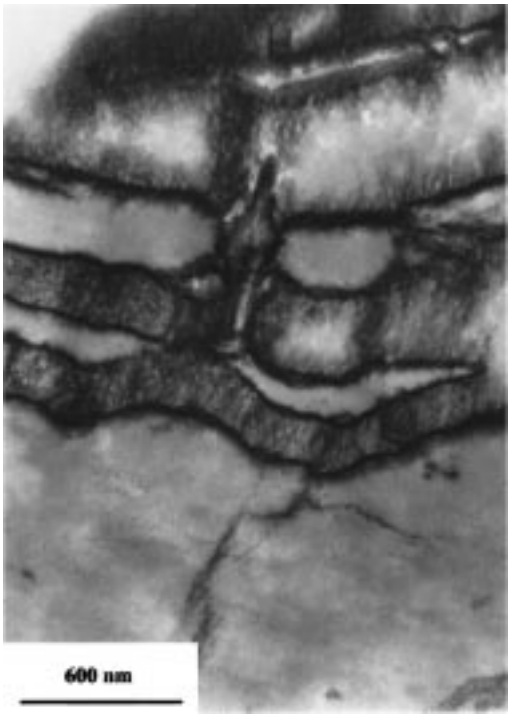


**Figure 15.** Detail from the edge of the main DZ in Figure 13b on the iPP/iPP-*g*-MA side of the interface, showing secondary fibrillar DZs.

Figure 16 shows the tip of the DZ, which propagated along the interface, indicating cavitation and fibrillation to occur in the early stages of deformation.

Figure 17 is a detail from the PA6 side of the interface behind the crack tip showing fibrillar debris. The

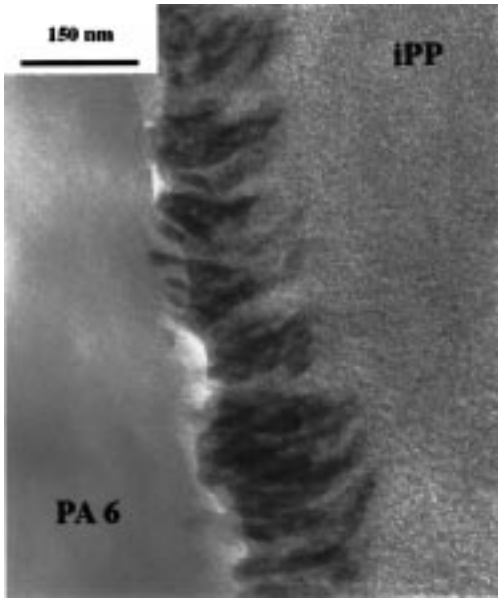


**Figure 16.** Detail from the tip of the DZ in Figure 13b.

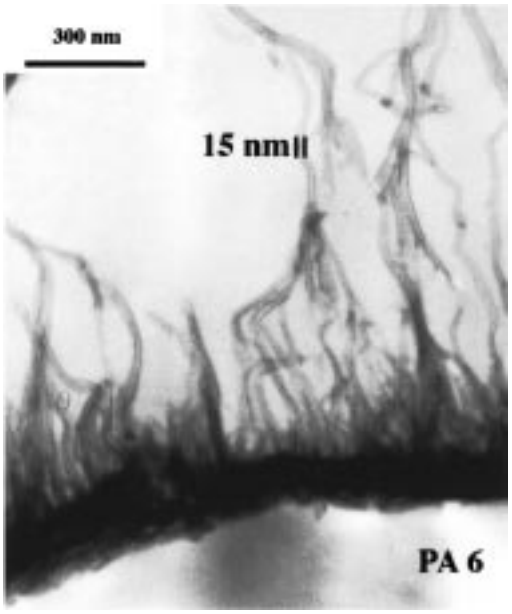


**Figure 17.** Fibrillar debris on the PA6 side of the interface, behind the crack tip in Figure 13b.

failure of the DZ during crack tip advance was always observed to occur at or close to the interface and no evidence for widespread deformation within the PA6 was seen, consistent with the results from the thin films. However, it is clear from Figure 17 that final failure did not involve a clean break between the iPP/iPP-*g*-MA and the PA6. Indeed certain fibrils appear to have broken down at distances of more than 100 nm from the interface. Images such as that in Figure 17 also allowed reliable estimation of the fibril thicknesses, which were confirmed to be of the order of 10 nm in both samples. However, as shown in Figures 18 and 19, the lower strength interface showed no diffuse deformation at the DZ edge, except where the DZ intercepted one of the inclusions referred to above, and as shown in Figure 18 (an undeformed inclusion is also visible in Figure 17). Moreover, little fibrillar debris was seen on the PA6 side of the interface behind the


**Figure 18.** Detail from the edge of the DZ in Figure 13a on the iPP/iPP-*g*-MA side of the interface, also showing a second phase inclusion.

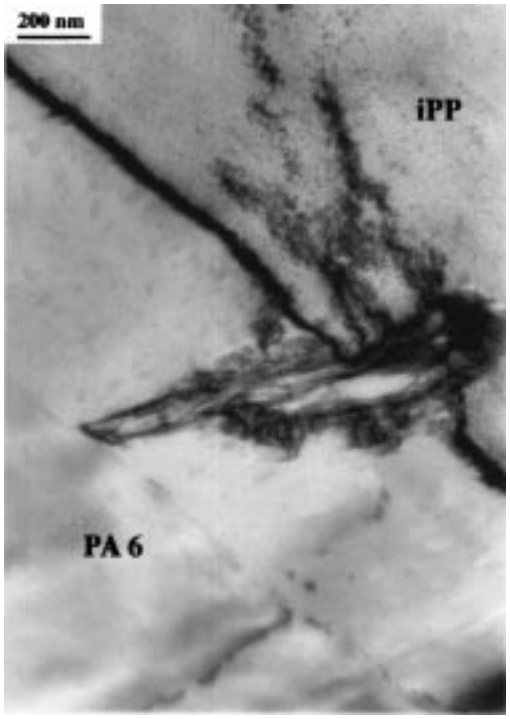


**Figure 19.** Detail from the DZ in Figure 13a showing a second phase inclusion which has been engulfed by the main DZ, resulting in relatively coarse cavitation and nucleation of diffuse deformation beyond the edge of the main DZ.

crack tip in the low strength interface. Consistent features were also seen in a second low strength interface ($G_c = 20$ J m$^{-2}$), namely, a well-defined single crack-tip DZ running along the interface and fracture at the (iPP/iPP-*g*-MA)−PA6 interface.

## Discussion

The width, $h_f$, of the main DZ at the crack tip was estimated from the TEM micrographs to be about 6 $\mu$m for the interface with $G_c = 300$ J m$^{-2}$ (although the total width of the damage zone was about twice this value if the diffuse deformation was taken into account). Assuming $\lambda = 4$, as in the thin films, then the DZ will have advanced at least 1.5 $\mu$m into the iPP/iPP-*g*-MA (that is a distance $h_f/\lambda$). This means that it will have engulfed the whole of the biaxially oriented layer referred to in the first part of the Results section and entered the mixed spherulitic transcrystalline zone depicted in Figure 9. As was also apparent from the micrographs, the region of diffuse deformation beyond the edge of the main DZ was therefore associated with the more disordered crosshatched lamellar texture associated with this zone. Hence the occurrence of multiple DZs beyond the edge of the main DZ may be accounted for in terms of locally weak regions (such as the boundaries between regions of differing lamellar orientation referred to at the end of the first part of the Results section) and/or local stress concentrations, as well as variations in the yield stress and mode of deformation as a function of the local lamellar orientation.

In the weaker interfaces, where $h_f \leq 2$ $\mu$m, the edge of the DZ had not reached the edge of the biaxially oriented layer. It might therefore be inferred that the onset of diffuse deformation coincides with the passage of the DZ from the biaxial layer to the mixed region. Since $h_f$ is proportional to $G_c$, it follows from this that for all samples with relatively low $G_c$, the conditions of a single fibrillar DZ at the crack tip and breakdown of this DZ at the interface are met, as required by eq 1. Moreover, if we take the thickness of the biaxially oriented layer to be 1 $\mu$m, then setting $h_f = \lambda$ and $\delta_c = \lambda(1 - 1/\lambda) = \lambda - 1 = 3$ $\mu$m and again taking $S_c = 25$ MPa, the upper limit to the range of validity of the model is anticipated to be $G_c = 75$ J m$^{-2}$. This compares with an apparent upper limit to the range in which $G_c$ scales as $\Sigma^2$ of about 100 J m$^{-2}$, which is reasonable agreement in view of the estimations involved.

If the model is valid, then eq 1 should provide a reasonable estimate of $G_c$ for weak interfaces. Taking $\lambda = 4$ as previously, the fibril spacing is

$$D_o = \lambda^{1/2} D \tag{3}$$

or $D_o = 20$ nm, for $D = 10$ nm. We also assume $S_c = 25$ MPa, $f_s = 10^{-9}$ N (for chain scission), and $\alpha = 40$, as in a PMMA craze. This last choice is hard to justify but should suffice as an order of magnitude estimate (the presence of interfibrillar links in the iPP DZs may be inferred from the micrographs). Equation 1 then gives

$$G_c = (2.4 \times 10^{-32})\Sigma^2 \tag{4}$$

which is the equation of the curve depicted in Figure 1. The extent of the agreement with the data is probably fortuitous since none of the quantities in eq 1 is precisely known, and additional factors such as the polydispersity and the possibility of chain slip may intervene. Nevertheless, we consider this strong evidence in favor of the idea that the rupture strength of the fibrils is directly proportional to the number of copolymer chains formed in situ at the interface.

For higher $G_c$, it is clear that the presence of substantial diffuse deformation beyond the main DZ in-

validates eq 1, but this does not explain the apparently anomalous data for longest/highest temperature heat treatments and higher molecular weight iPP-*g*-MA. Although increased delocalization of the crack tip deformation should increase $G_c$ for a given $\Sigma$, it has not so far been possible to identify any major differences in microstructure between these samples and those with lower $G_c$, so that one might expect a priori all samples with the same $\Sigma$ to display similar toughness. Although evidence from X-ray scattering for the presence of the iPP $\beta$ phase close to the interface has been invoked previously to account for enhanced toughening,[18] its presence close to relatively strong interfaces has not been confirmed by the present work. Although any difference in yield stress between the $\alpha$ and $\beta$ phases alone would not provide an explanation for the up to 4-fold increases in $G_c$ for a given $\Sigma$, seen in certain samples (cf. Figure 1), it is possible that a certain amount of $\beta$ phase is associated with microstructures which show a greater tendency toward diffuse deformation at the crack tip.

The nature of the interface itself may also be important, but the present methods of observation make it difficult to obtain precise information concerning the interphase thickness and/or the interfacial morphology at high resolution, owing to the systematic variations in the appearance of the interface with different degrees of staining. It is nevertheless worth mentioning that no evidence was found for micelle formation at the interface, this representing one potential difference between interfaces heat treated at low and high temperatures. There have been reports of micelle formation at the interface in similar systems,[50] but the samples in question were melt processed blends, whereas in the present case, melting of the PA6 was only partial. Indeed micelles have also been observed in moderately stained reaction bonded (iPP/iPP-*g*-MA)−PA6 interfaces, but only for significantly higher heat treatment temperatures than those employed here (240 °C).[51]

## Conclusions

The basic assumptions behind Brown's model linking macroscopic fracture toughness to parameters governing microdeformation at the crack tip in glassy polymers appear to be justified for the (iPP/iPP-*g*-MA)−PA6 interfaces described here, provided $G_c$ is less than about 100 J m$^{-2}$. The observed fibril sizes in these DZs were about 10 nm, and for a reasonable choice of the remaining parameters in Brown's expression for $G_c$, good agreement with the experimental data was obtained. For larger $G_c$, deformation at the crack tip appeared more diffuse both in bulk samples and in thin films. In the bulk samples, this was argued to be because the crack tip DZ extended laterally beyond the limits of a biaxially oriented layer of about 1 $\mu$m in thickness and into a region of more heterogeneous microstructure, where the presence of local weak spots may have promoted the observed multiple DZ formation. Although this would explain why the model fails to describe the evolution of $G_c$ above about 100 J m$^{-2}$, it does not explain why interfaces heat treated at high temperature have relatively high interfacial strengths for a given $\Sigma$.

**Acknowledgment.** We acknowledge the staff and facilities of the Interdepartmental Electron Microscopy Centre of the EPFL.

## References and Notes

(1) Char, K.; Brown, H. R.; Deline, V. R. *Macromolecules* **1993**, *26*, 4164.
(2) Brown, H. R.; Char, K.; Deline, V. R.; Green, P. F. *Macromolecules* **1993**, *26*, 4155.
(3) Norton, L. J.; Smigolova, V.; Pralle, M. U.; Hubenko, A.; Dai, K. H.; Kramer, E. J.; Hahn, S.; Berglund, C.; DeKoven, B. *Macromolecules* **1995**, *28*, 1999.
(4) Brown, H. R.; Deline, V.; Green, P. F. *Nature* **1989**, *341*, 221.
(5) Creton, C.; Kramer, E. J.; Hui, C.-Y.; Brown, H. R. *Macromolecules* **1992**, *25*, 3075.
(6) Brown, H. R. *Macromolecules* **1989**, *22*, 2859.
(7) Kramer, E. J.; Norton, L. J.; Dai, C. A.; Sha, Y.; Hui, C. Y. *Faraday Discuss.* **1994**, *98*, 31.
(8) Washiyama, J.; Creton, C.; Kramer, E. J. *Macromolecules* **1992**, *25*, 4751.
(9) Dai, C.-A.; Dair, B. J.; Dai, K. H.; Ober, C. K.; Kramer, E. J.; Hui, C.-Y.; Jelinski, L. W. *Phys. Rev. Lett.* **1994**, *73*, 2472.
(10) Creton, C.; Kramer, E. J.; Hadziioannou, G. *Macromolecules* **1991**, *24*, 1846.
(11) Brown, H. R. *Macromolecules* **1991**, *24*, 2752.
(12) Sha, Y.; Hui, C. Y.; Ruina, A.; Kramer, E. J. *Macromolecules* **1995**, *28*, 2450.
(13) Xu, D. B.; Hui, C. Y.; Kramer, E. J.; Creton, C. *Mech. Mater.* **1991**, *11*, 257.
(14) Hui, C. Y.; Ruina, A.; Creton, C.; Kramer, E. J. *Macromolecules* **1992**, *25*, 3948.
(15) Xiao, F.; Hui, C. Y.; Kramer, E. J. *J. Mater. Sci.* **1993**, *28*, 5620.
(16) Xiao, F.; Hui, C. Y.; Washiyama, J.; Kramer, E. J. *Macromolecules* **1994**, *27*, 4382.
(17) Boucher, E.; Folkers, J. P.; Hervet, H.; Leger, L.; Creton, C. *Macromolecules* **1996**, *29*, 774.
(18) Boucher, E.; Folkers, J. P.; Creton, C.; Hervet, H.; Léger, L. *Macromolecules* **1997**, *30*, 2102.
(19) Behan, P.; Bevis, M.; Hull, D. *Philos. Mag.* **1971**, *24*, 1261.
(20) Lauterwasser, B. D.; Kramer, E. J. *Philos. Mag.* **1979**, *39A*, 469.
(21) Kramer, E. J.; Berger, L. L. In *Advances in Polymer Science 91/92*; Kausch, H.-H., Ed.; Springer-Verlag: Berlin, 1990; Chapter 1.
(22) Kramer, E. J. In *Advances in Polymer Science 52/53*; Kausch, H.-H., Ed.; Springer-Verlag: Berlin, 1983; Chapter 1.
(23) Dettenmaier, M. In *Advances in Polymer Science 52/53*; Kausch, H.-H., Ed.; Springer-Verlag: Berlin, 1983; Chapter 2.
(24) Brown, H. R.; Kramer, E. J. *J. Macromol. Sci. Phys.* **1981**, *B19*, 487.
(25) Behan, P.; Bevis, M.; Hull, D. *Proc. R. Soc.* **1975**, *A434*, 525.
(26) Berger, L. L. *Macromolecules* **1989**, *22*, 3162.
(27) Yang, A. C.-M.; Kramer, E. J. *J. Polym. Sci., Polym. Phys. Ed.* **1985**, *23*, 1353.
(28) Miller, P.; Buckley, D. J.; Kramer, E. J. *J. Mater. Sci.* **1991**, *26*, 4445.
(29) Hui, C. Y.; Kramer, E. J. *Poly Sci. Eng.* **1995**, *35*, 419.
(30) Brown, H. R.; Char, K.; Deline, V. R. In *Block Copolymers and Adhesion Between Immiscible Polymers*; Brown, H. R., Char, K., Deline, V. R., Eds.; Elsevier: New York, 1991; Vol. 5, p 51.
(31) Washiyama, J.; Kramer, E. J.; Hui, C.-Y. *Macromolecules* **1993**, *26*, 2928.
(32) Washiyama, J.; Creton, C.; Kramer, E. J.; Xiao, F.; Hui, C.-Y. *Macromolecules* **1993**, *26*, 6011.
(33) Plummer, C. J. G.; Kausch, H.-H. *Macromol. Chem. Phys.* **1996**, *197*, 2047.
(34) Smith, G. D.; Toll, S.; Månson, J.-A. E. In *Proc. Flow Processes in Composite Materials*; Galway, Ireland, July 7−9, 1994.
(35) Olf, H. G.; Peterlin, A. J. *J. Polym. Sci., Polym. Phys. Ed.* **1974**, *12*, 2209.
(36) Olf, H. G.; Peterlin, A. J. *Macromolecules* **1973**, *6*, 470.
(37) Jang, B. Z.; Uhlmann, D. R.; Van der Sande, J. B. *Polym. Eng. Sci.* **1985**, *25*, 98.
(38) Wolfe, S.; Hasan, S. K.; Campbell, J. R. *Chem. Commun.* **1970**, 1420.
(39) Lutz, C. Ph.D. Thesis, University of Stuttgart, 1991.
(40) Turner-Jones, A.; Aizlewood, J. M.; Beckett, D. R. *Makromol. Chem.* **1968**, *75*, 134.
(41) Holmes, D. R.; Bunn, C. W.; Smith, D. J. *J. Polym. Sci.* **1955**, *17*, 159.
(42) Keller, A. *J. Polym. Sci.* **1955**, *17*, 351.
(43) Olley, R. H.; Bassett, D. C. *Polymer* **1989**, *30*, 399.
(44) Olley, R. H.; Bassett, D. C. *Polymer* **1982**, *23*, 1707.

(45) Norton, D. R.; Keller, A. *Polymer* **1985**, *26*, 704.
(46) Keith, H. D.; Padden, F. J.; Walker, N. M.; Wyckoff, H. W. *J. Appl. Phys.* **1959**, *30*, 1485.
(47) Lotz, B.; Wittmann, J. C. *J. Polym. Sci., Polym. Phys. Ed.* **1986**, *24*, 1541.
(48) Petermann, J. In *Polypropylene: structure, blends and composites*; Karger-Kocsis, J., Ed.; Chapman and Hall: London, 1995.
(49) Plummer, C. J. G.; Smith, G. D. Unpublished work, Lausanne, 1996.
(50) Li, H.; Chiba, T.; Higashida, N.; Yang, Y.; Inoue, T. *Polymer* **1997**, *38*, 3921.
(51) Smith, G. D. Ph.D. Thesis, Ecole Polytechnique Fédérale de Lausanne, 1997.

MA971852V